Title	Dislocation plasticity in c-axis nanopillar compression of wurtzite ceramics: A study using neural network potentials
Author(s)	Zhang, Shihao; Ogata, Shigenobu
Citation	Journal of the American Ceramic Society. 2025, p. e20406
Version Type	VoR
URL	https://hdl.handle.net/11094/100546
rights	This article is licensed under a Creative Commons Attribution 4.0 International License.
Note	

Journal
American Ceramic Society

Dislocation plasticity in *c*-axis nanopillar compression of wurtzite ceramics: A study using neural network potentials

Shihao Zhang 🄳 | Shigenobu Ogata 🄳

Department of Mechanical Science and Bioengineering, Graduate School of Engineering Science, Osaka University, Osaka, Japan

Correspondence
Shigenobu Ogata, Department of Mechanical Science and Bioengineering, Graduate School of Engineering Science, Osaka University, Osaka, 560-8531, Japan.
Email: ogata@me.es.osaka-u.ac.jp

Abstract

Ceramics typically exhibit brittle characteristics at room temperature. However, under high compressive stress conditions, such as during nanoindentation or compression tests on nanopillars, these materials can reach the necessary shear stress for dislocation nucleation and glide before fracture occurs. This allows for the observation of plastic deformation through dislocations even at room temperature. Yet, detailed insights into their atomic-scale dislocation plasticity remain scarce. This study employs atomistic simulations to explore the dislocation plasticity in *c*-oriented nanopillars of wurtzite ceramics (i.e., GaN and ZnO) under uniaxial [0001] compression, utilizing a specially developed first-principles neural network interatomic potential. We observed activation of $\{01\bar{1}1\}\langle 11\bar{2}3\rangle$ and $\{11\bar{2}2\}\langle 11\bar{2}3\rangle$ dislocations, corroborating experimental findings from in-situ compression tests. Moreover, a wurtzite-to-hexagonal phase transformation begins at facet edges and extends inward, forming wedge-shaped regions. As compression progresses, dislocations nucleate at the wurtzite-hexagonal phase boundary and spread throughout the nanopillar, contributing to a rougher surface texture. These quantitative results offer new insights into the plastic deformation behaviors of nanopillars under compressive loading, highlighting the potential of dislocation engineering in these ceramics.

KEYWORDS
dislocation plasticity, nanopillar, neural network potential, phase transformation, semiconductor

1 | INTRODUCTION

Topological one-dimensional defect, known as dislocation, is gaining prominence in both structural and functional ceramics due to their potential in "dislocation engineering."[1–10] The critical role of dislocations in plastic deformation and the toughening of both bulk and nanoscale ceramics is gaining increasing attention, such as bulk UO_2[11–13] and nanocube MgO[14–17] that reveal a site-dependent nature of surface dislocation nucleation. Dislocation in ceramics, which exhibit non-stoichiometry, excess core charge, and localized strain fields, can significantly modify the mechanical and functional properties of ceramics, making them vital for next-generation device applications.[1–10] Such capabilities include enhanced plasticity,[6] anisotropic thermal transport,[7] tunable ferroelectricity,[8,9] and improved photoconductivity.[10]

In particular, wurtzite ceramics of GaN and ZnO, both direct wide bandgap semiconductors,[18] are becoming increasingly recognized for their potential in various device applications through dislocation engineering. As interest grows in utilizing GaN and ZnO in nanoscaled devices for nanoelectronic components[19] and micro- and nanoscale transistors,[20] the ability to precisely engineer and control dislocations within these devices is proving crucial. These mechanical properties, especially those related to dislocation plasticity, are fundamental for device fabrication, processing, and optimizing operational performance.

Although wurtzite GaN and ZnO are typically brittle at the bulk scale, they can exhibit room-temperature plastic deformation at smaller scales under compressive loading conditions found in nano- and micro-pillar compression tests[21–24] and nanoindentation tests.[25,26] In-situ compression tests on GaN and ZnO nano- and micro-pillars were conducted within high-resolution electron microscopes, facilitating real-time observation of structural changes during deformation. These experiments offer invaluable insights into the mechanisms of deformation, such as the initiation and propagation of dislocations, shear bands, and cracks, along with their precise timing and spatial distribution. Notably, in-situ TEM compression tests on GaN pillars, with diameters ranging from ∼200 to 700 nm, have demonstrated that plastic deformation is primarily driven by the formation of slip bands on the $(01\bar{1}1)$ plane.[21,22] Additionally, deformation has been observed to proceed through second-order pyramidal slip along the $\{11\bar{2}2\}\langle11\bar{2}3\rangle$ slip system during in-situ micropillar compression.[23,24] For ZnO micropillars, microcompression tests reveal that the primary slip plane forms an acute angle of 62° with the basal plane, indicative of pyramidal slip.[27]

Despite real-time observations of deformation-induced structural changes in in-situ microcompression tests, achieving a detailed atomic-scale understanding of dislocation plasticity remains challenging. This limitation arises primarily due to technical constraints in both experimental setups and simulation capabilities. On the experimental side, challenges include the need for precisely prepared samples and advanced ultramicroscopy with high spatial resolution capable of resolving dislocation core structures.[28,29] On the simulation front, while density functional theory (DFT) provides reliable results, it is constrained by computational limits on model size. This restriction makes it difficult to perform large-scale atomic simulations that are necessary to accurately capture complex dislocation processes. In contrast, classical molecular dynamics (MD) simulations can handle systems with millions of atoms on a nanosecond timescale. However, the major challenge in realistic MD simulations

lies in developing a reliable interatomic potential that can accurately model the intricate interactions inherent in these materials.

In this work, we employed our first-principles neural network interatomic potential (NNIP)[30] to perform MD simulations, investigating the dislocation plasticity of single-crystal GaN and ZnO nanopillars under uniaxial compression along the [0001] direction. It is revealed that the wurtzite ceramics of GaN and ZnO exhibit similar dislocation plasticity in c-oriented nanopillar compression. During the compression process, $\{01\bar{1}1\}\langle11\bar{2}3\rangle$ and $\{11\bar{2}2\}\langle11\bar{2}3\rangle$ dislocations were activated, which is consistent with results from in-situ compression experiments. In detail, the transformation from wurtzite to hexagonal phase occurs at the facet edges, creating wedge-shaped regions that progressively extend inward as compression increases. Dislocations subsequently nucleate at the phase boundary of the wurtzite and hexagonal phases and propagate throughout the nanopillars, leading to a rougher surface texture. These findings provide crucial insights for advancing dislocation engineering in nanodevices of wurtzite ceramics. In this manuscript, GaN results are primarily presented to illustrate the dislocation configuration and dislocation nucleation in c-oriented nanopillar compression of wurtzite ceramics, while ZnO results are briefly discussed for comparison.

2 | METHODS

2.1 | Molecular dynamics simulation

All MD simulations were performed using the Large-scale Atomic/Molecular Massively Parallel Simulator (LAMMPS) code,[31] paired with our previously developed first-principles NNIP for the dislocation plasticity in ceramics.[30] This potential provides accuracy comparable to first-principles calculations but at a lower computational cost. The accuracy and performance of the potential were validated across various properties, including lattice constants, elastic constants, elastic moduli, phonon dispersion, surface energy, energy under volumetric strain, cleavage energy, formation energy of planar defects, stacking fault energy, dislocation core structure, and dislocation slip barrier. For comprehensive details on the training dataset and validation results, please refer to our prior publications.[30] The atomic configurations of dislocation were analyzed and visualized with the Identify Diamond Structure (IDS)[32] and Dislocation Extraction Algorithm (DXA)[33] tools of the OVITO program.[34] To visualize the strain distribution at the atomic scale, the atomic von Mises strain η_i^{Mises}[35] was computed based on the atomic strain tensor η_i.[36] The simulations were conducted
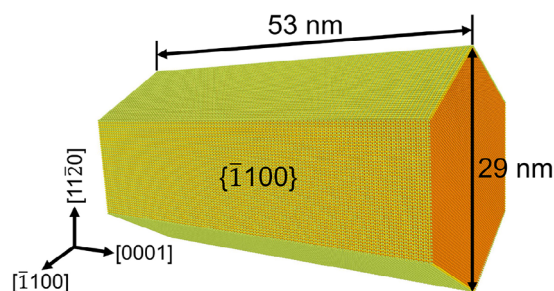
FIGURE 1 Model of a *c*-oriented GaN and ZnO nanopillar in the wurtzite phase with a hexagonal cross-sectional shape, six {$\bar{1}$100}-type lateral crystalline surfaces, and a [0001] axial orientation. Atoms are color-coded by the Identify Diamond Structure (IDS) method.[32]

on a single node of the SQUID supercomputer[37] at the Cybermedia Center, Osaka University, equipped with two Intel Xeon Platinum 8368 processors and eight NVIDIA A100 GPUs. Each nanopillar compression simulation, consisting of approximately 300 000 timesteps, typically required around 50 h to complete.

2.2 | Nanopillar compression simulation

The *c*-oriented nanopillars are in the wurtzite phase with a hexagonal cross-sectional shape, six {$\bar{1}$100}-type lateral crystalline surfaces, and a [0001] axial orientation (see Figure 1), which has been widely prepared in experiment.[38–42] The nanopillar models, measuring 29 nm in diameter and 53 nm in length, comprise approximately 2.3 million atoms. The length-to-lateral dimension ratio was set to approximately 2:1 to avoid buckling. The models are periodic along the [0001] direction. The model was relaxed using the NPT ensemble at a temperature of 300 K and a timestep of 0.001 ps for 50 ps to release the stress along the [0001] direction. Subsequently, a uniaxial compressive load was applied by linearly rescaling the system length in the [0001] direction under an NVT ensemble at 300 K. The strain rate was initially set to 5×10^8 s^{-1} and was reduced to 5×10^7 s^{-1} as the system approached the onset of plastic response of phase transformation and dislocation nucleation.

Since the plastic deformation of nanopillars typically initiates from the surface, the atomic-level details of the surfaces are critical. Our NNIP accurately describes the surface energy and relaxed surface structures of ZnO and GaN.[30] The surface details in the nanopillar model were analyzed after relaxation in the NPT ensemble at 300 K for 50 ps, as shown in Figure S1 in the Supporting Information. It was observed that the configuration of the prismatic surface closely resembles the bulk stacking but exhibits slight rumpling and displacement in the

topmost layers. This behavior aligns with the fact that nonpolar prismatic planes do not undergo complex surface reconstructions induced by surface vacancies or adatoms but instead show slight rumpling and displacement in the topmost layers, as demonstrated in experiments.[43,44]

A nanopillar compression simulation was also performed on a circular model with a diameter of 26 nm and a length of 53 nm. As shown in Figure S2 in the Supporting Information, the results exhibit dislocation plasticity similar to that of the hexagonal nanopillar. Therefore, the subsequent discussion centers on the hexagonal nanopillar as the prototype. Furthermore, in many previous simulation studies on nanopillar compression,[45] nonperiodic models were employed, with one side fixed and the other left as a free surface where the compressive load was applied. However, in most nanopillar or micropillar samples, which are elongated with smaller cross sections, plastic deformation—such as dislocation nucleation—typically originates from the free surfaces on the sides rather than from the top surface in contact with the flat punch.[27,46,47] In such cases, a periodic model employed in this work is more suitable. This contrasts with samples having a small length-to-diameter ratio, such as nanocubes,[14–17] where the free top surface in contact with the flat punch plays a crucial role in their plastic deformation, necessitating the use of a nonperiodic model.

Figure 2 illustrates the typical deformation directions on the basal {0001}, prismatic I {10$\bar{1}$0}, prismatic II {11$\bar{2}$0}, pyramidal I {10$\bar{1}$1}, and pyramidal II {11$\bar{2}$2} planes in the wurtzite structure. The relaxed lattice constants for GaN obtained by our NNIP are $a = 3.224$ Å and $c = 5.290$ Å, aligning well with the DFT results of $a = 3.248$ Å and $c = 5.282$ Å, and experimental measurements of $a = 3.190$ Å and $c = 5.189$ Å.[48] For ZnO, the NNIP provides relaxed lattice constants of $a = 3.287$ Å and $c = 5.305$ Å, also aligning well with the DFT results of $a = 3.287$ Å and $c = 5.306$ Å, and experimental measurements of $a = 3.25$ Å and $c = 5.21$ Å.[49] The Pyramidal I planes, parallel to the $\langle 11\bar{2}0 \rangle$ direction, form an angle of 62.2° from the basal plane for GaN and 61.8° for ZnO. The Pyramidal II planes, aligned with the $\langle 1\bar{1}00 \rangle$ direction, form an angle of 58.6° for GaN and 58.2° for ZnO with the basal plane.

2.3 | Compressive simulation using density functional theory

The stress–strain curves of unit cells under uniaxial [0001] compressive deformation were calculated using our developed ADAIS code,[50] in conjunction with DFT calculations, to verify the reliability of the NNIP model, particularly its prediction of the wurtzite-to-hexagonal phase
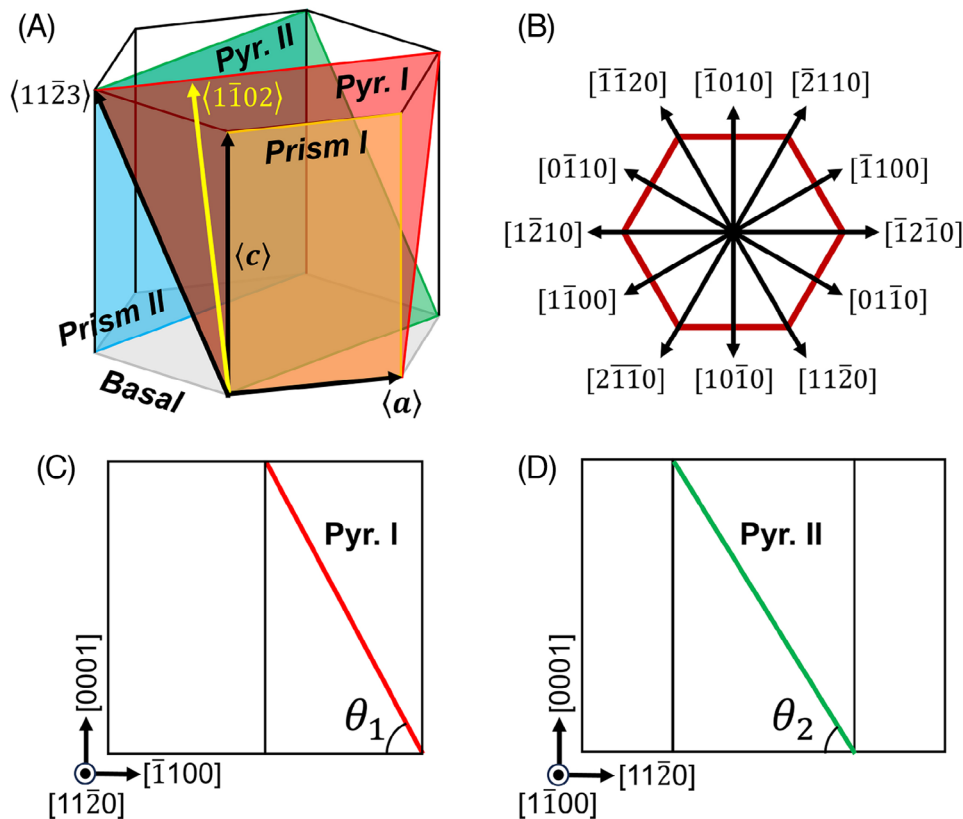
FIGURE 2 (A) Typical slip systems on the basal {0001}, prismatic I {10$\bar{1}$0}, prismatic II {11$\bar{2}$0}, pyramidal I {10$\bar{1}$1}, and pyramidal II {11$\bar{2}$2} planes in the wurtzite structure. The vector ⟨1$\bar{1}$02⟩ is perpendicular to ⟨11$\bar{2}$0⟩ on the pyramidal I plane. (B) A top-down view of the (0001) plane of a hexagonal lattice cell. (C–D) The hexagonal lattice cell projected along (C) [11$\bar{2}$0] and (D) [1$\bar{1}$00]. The angles θ_1 and θ_2 of pyramidal I and II planes from the basal plane are 62.2° and 58.6° for GaN with the NNIP relaxed lattice constants of a = 3.224 Å and c = 5.290 Å, as well as 61.8° and 58.2° for ZnO with the NNIP relaxed lattice constants a = 3.287 Å and c = 5.305 Å, respectively.

transformation under compressive loading. DFT calculations were carried out using the Vienna ab initio simulation package (VASP) code.[51] The projector-augmented wave (PAW) method[52] was employed, alongside the Perdew–Burke–Ernzerhof (PBE) version[53] of the generalized gradient approximation (GGA) for the exchange-correlation functional. An energy cutoff of 520 eV was set, with an energy convergence criterion of 10^{-6} eV/cell. The Gaussian method[54] with a smearing width of 0.01 eV was used for the electronic self-consistency calculations. Ionic relaxation was subject to a force convergence criterion of 10^{-3} eV/Å. The Monkhorst–Pack k-mesh[55] approach was utilized, employing 6000 k-points per reciprocal atom (KPPRA).[56,57]

3 | RESULTS AND DISCUSSION

In the in-situ compression tests on c-oriented GaN micropillars and nanopillars,[21–24] both {01$\bar{1}$1}⟨11$\bar{2}$3⟩ and {11$\bar{2}$2}⟨11$\bar{2}$3⟩ dislocations were observed to activate during compression. Magagnosc et al.[24] reported that the initial dislocations formed in compressed c-oriented GaN micropillars were 1/3⟨11$\bar{2}$3⟩{11$\bar{2}$2} dislocations, which make an angle of approximately 57° with the basal plane. Similarly, Wheeler et al.[23] identified the primary deformation mechanism in samples with a hexagonal cross section, characterized by six {01$\bar{1}$0}-type lateral crystalline surfaces, as slipping along the second-order pyramidal {11$\bar{2}$2} plane in the ⟨11$\bar{2}$3⟩ direction. In these samples, slip planes were observed to initiate at the edges of the facets rather than directly on the facets. Slip along the first-order pyramidal {10$\bar{1}$1} plane, which is oriented at an acute angle of 62° to the basal plane {0001},[22] has also been observed. This finding is consistent with the observations reported by Fan et al.[21] However, given that the angular accuracy of these measurements is limited to approximately 1–2°, distinguishing between the {10$\bar{1}$1}⟨11$\bar{2}$3⟩ and {11$\bar{2}$2}⟨11$\bar{2}$3⟩ slip systems based on angular measurements alone remains challenging, as they form angles of 62.2° and 58.6° from the basal plane, respectively (see Figures 2C–D).

Figures 3A–D illustrate the atomic and dislocation configurations at a compressive engineering strain of ε_{zz} = −0.1157, projected along [1$\bar{1}$00] and [0$\bar{1}$10] directions. The
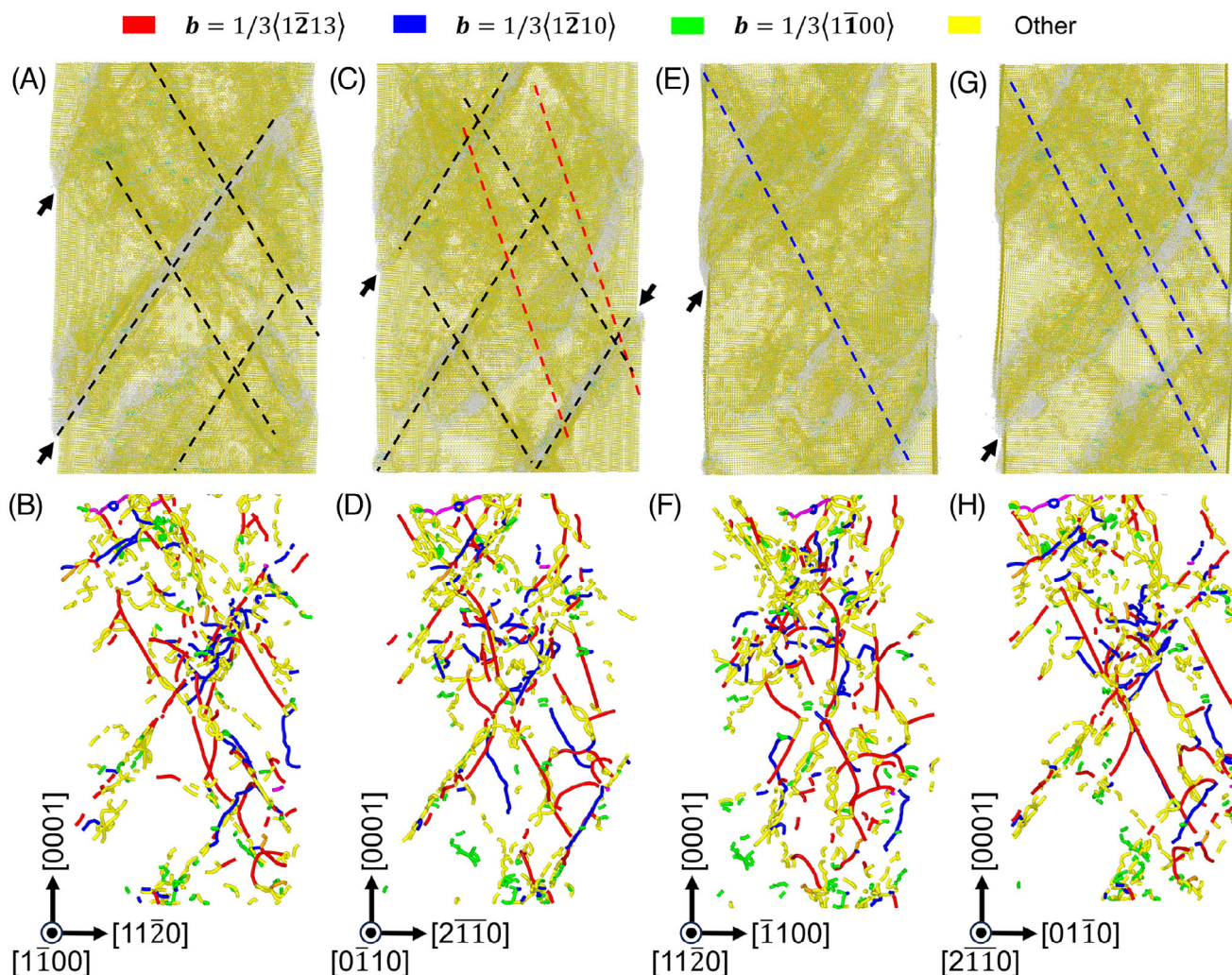
FIGURE 3 Snapshots of atomic configurations for GaN under a compressive engineering strain of $\varepsilon = -0.1157$, projected along (A–B) $[1\bar{1}00]$, (C–D) $[0\bar{1}10]$, (E–F) $[11\bar{2}0]$, and (G–H) $[2\bar{1}\bar{1}0]$. See Figure 2B for the orientation relationship. They were analyzed via (A, C, E, G) the Identify Diamond Structure (IDS) method,[32] and (B, D, F, H) the Dislocation Extraction Algorithm (DXA)[33] based on the Ga HCP sublattice. The slip planes are highlighted by black, red, and blue dashed lines, with angles of approximately 58°, 70°, and 62° from the basal plane, respectively. Atoms within perfect wurtzite structures are not shown in (A, C, E, G).

$1/3\langle 1\bar{2}13\rangle$ dislocations are activated on slip planes aligned with the $\langle 1\bar{1}00\rangle$ direction, forming an angle of approximately 58° with respect to the basal plane, as highlighted by black dashed lines in Figures 3A and C. This indicates that the active slip system is on the pyramidal II plane, aligning well with experimental results.[23,24] Furthermore, a secondary slip band oriented at approximately 72° relative to the basal plane, with a Burgers vector of $1/3\langle 1\bar{2}13\rangle$, has been observed experimentally.[24] This orientation does not correspond to any major slip system in GaN. However, similar secondary slip planes, highlighted by red dashed lines in Figure 3C, were also observed in the simulations. These secondary slip planes, also on pyramidal II planes but not parallel to the viewing direction $[0\bar{1}10]$, show an angle of approximately 70° from the basal plane. Our simulation results offer a plausible interpretation for the experimentally observed secondary slip bands.[24]

From the atomic configuration snapshots projected along the $[11\bar{2}0]$ and $[2\bar{1}\bar{1}0]$ directions, as depicted in Figures 3E–H, $1/3\langle 11\bar{2}3\rangle$ dislocations on the pyramidal I plane are evident. These dislocations align with the $\langle 11\bar{2}0\rangle$ direction and form an angle of 62° with the basal plane, corroborating previous experimental findings.[21,22] In addition to the $1/3\langle 11\bar{2}3\rangle$ dislocation, the $\langle 11\bar{2}0\rangle$ edge dislocations on pyramidal I plane are also observed (highlighted by blue lines in Figure 3). The corresponding dislocation cores extracted from the snapshots of GaN nanopillar compression simulation are shown in Figure 4, including pyramidal I $\langle 11\bar{2}3\rangle$ edge dislocation, pyramidal II $\langle 11\bar{2}3\rangle$ edge dislocation, $\langle 11\bar{2}3\rangle$ screw dislocation, and pyramidal I $\langle 11\bar{2}0\rangle$ edge dislocation.
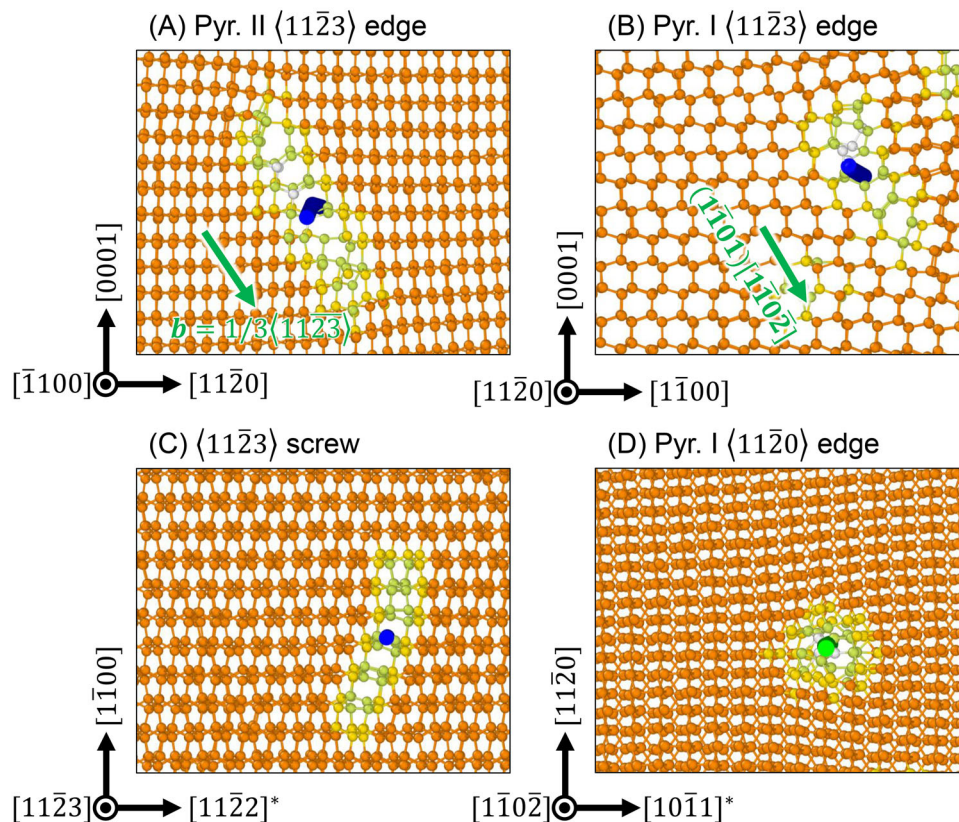
FIGURE 4 The dislocation cores extracted from the snapshots of GaN nanopillar compression simulation: (A) pyramidal II $\langle 11\bar{2}3 \rangle$ edge dislocation, (B) pyramidal I $\langle 11\bar{2}3 \rangle$ edge dislocation, (C) $\langle 11\bar{2}3 \rangle$ screw dislocation, and (D) pyramidal I $\langle 11\bar{2}0 \rangle$ edge dislocation. It is noted that these dislocation cores may not be in an equilibrium state. The vector $[1\bar{1}0\bar{2}]$ is perpendicular to $[11\bar{2}0]$ on the pyramidal I plane, as defined in Figure 2A. Atoms are color-coded by the structure types analyzed via the Identify Diamond Structure (IDS) method,[32] and the dislocation lines are also shown by blue and green lines for the $\langle 11\bar{2}3 \rangle$ and $\langle 11\bar{2}0 \rangle$ dislocations, respectively, analyzed by the Dislocation Extraction Algorithm (DXA)[33] based on the Ga HCP sublattice.

During the [0001] compression of a c-oriented GaN nanopillar at an engineering strain of $\varepsilon_{zz} = -0.1155$, the transformation from wurtzite to hexagonal phase initiates at a facet edge, highlighted by black arrows in Figure 5B, forming wedge-shaped regions at an approximate angle of 50° to the basal plane. Figure 6 displays the stress–strain curve for wurtzite GaN unit cell under uniaxial [0001] compression, indicating a breakpoint at a compressive engineering strain of $\varepsilon_{zz} = -0.1700$, aligning with the onset of the wurtzite-to-hexagonal phase transformation. To substantiate this observation, corresponding DFT results are included in Figure 6, showing robust agreement with the NNIP outcome.

Under ambient conditions, GaN possesses a wurtzite lattice structure, depicted in Figure 6A. This structure features tetrahedral bonding with a coordination number of 4, characterized by N-Ga-N or Ga-N-Ga bonding angles of 109.5°. When subjected to uniaxial [0001] compression, Ga cations and N anions located on the (0001) plane are inclined to move toward each other and form bonds, as illustrated in Figure 6B. Consequently, a new Ga-N bond is established along the [0001] direction, while three

of the four original tetrahedral Ga-N bonds not aligned with [0001] are compressed flat within the {0001} plane. This leads to the formation of a hexagonal lattice with a coordination number of 5 and two distinct types of bonding angles, marking the wurtzite-to-hexagonal transformation. The first type is a 90° bonding angle, made up of two Ga-N bonds along the [0001] and [000$\bar{1}$] orientations, respectively. The second type consists of three Ga-N bonds that mutually form a 120° bonding angle within the {0001} plane, as shown in Figure 6B.

In contrast to nanoindentation tests, where stress is localized, nanopillar compression results in a generally uniform stress field. This uniformity allows phase transformations and dislocation nucleation to occur throughout the sample, including at free surfaces and edges. In dislocation-free nanopillars, plastic deformation occurs through stochastic surface dislocation nucleation events, interspersed with periods of inactivity that depend on the availability of surface defects. Consequently, the pristine c-oriented GaN nanopillar in this study displays multiple nucleation sites, resulting in several distinct regions of phase transformation that increasingly grow inward into
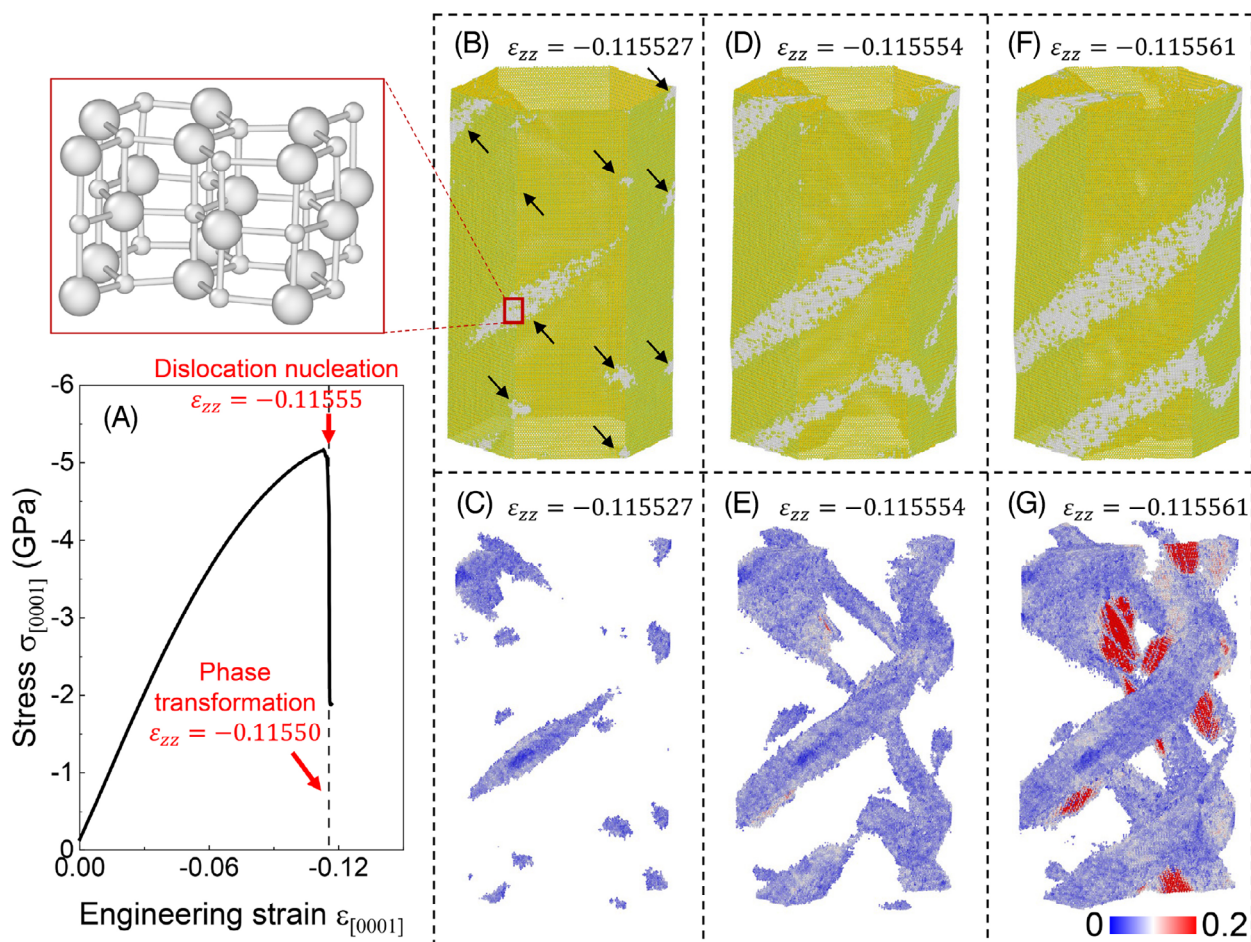
FIGURE 5 (A) The curve of the stress $\sigma_{[0001]}$ versus engineering strain $\varepsilon_{[0001]}$ of c-oriented nanopillar compression for GaN. (B–G) Snapshot of MD simulation showing the wurtzite-to-hexagonal phase transition and dislocation nucleation, where atoms are color-coded by (B,D,F) structure types analyzed via the Identify Diamond Structure (IDS) method[32] and (C,E,G) atomic von Mises strain. To clarify, atoms on perfect wurtzite lattice are not shown in (B–G) and the surface atoms are not shown in (C,E,G). The wurtzite-to-hexagonal phase transformation is highlighted at the red rectangle in (B).
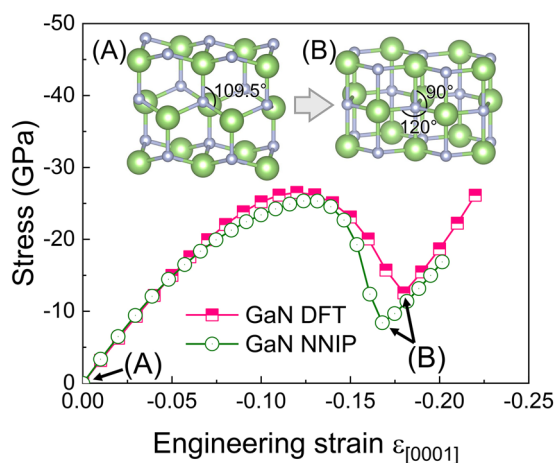

FIGURE 6 The calculated stress–strain curves of GaN unit cell under uniaxial [0001] compressive deformation via NNIP and DFT, together with (A–B) the snapshots of the deformed bonding structure with the engineering strain (A) $\varepsilon_{[0001]} = 0.0000$ and (B) $\varepsilon_{[0001]} = -0.1700$ (NNIP) and -0.1800 (DFT).

the sample under higher compression, as illustrated in Figures 5D–E. It is important to note that the critical [0001] compressive engineering strain (−0.1155) and peak stress (−5.06 GPa) at which phase transformation begins at the surface in the nanopillar (see Figure 5A) are significantly lower than those calculated for a unit cell (−0.1700 for strain and −25.33 GPa for peak stress) shown in Figure 6.

Figure 5G displays a snapshot from the MD simulation at a compressive engineering strain of −0.1156, with atoms color-coded according to atomic von Mises strain. At this strain level, which corresponds to a compressive stress of −5.06 GPa, dislocation nucleation, appearing in a half-loop configuration, is observed at the wurtzite-hexagonal phase boundary. The regions of dislocation nucleation exhibit significantly higher atomic von Mises strains compared to the rest of the phase transformation area. Figures 7, 8 illustrate the intricate process of dislocation nucleation at the wurtzite-hexagonal phase boundary. Dislocations nucleate on both the pyramidal I and pyramidal II planes, each with
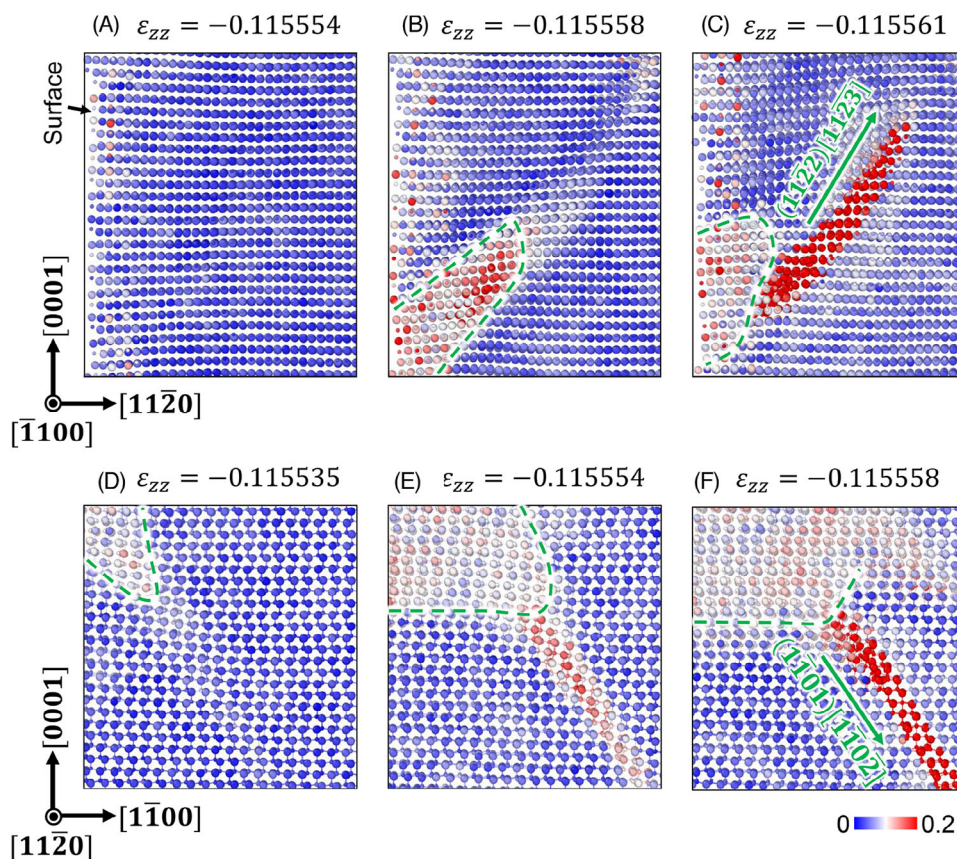
FIGURE 7 Snapshots of MD simulation for GaN showing (A–C) the nucleation of $(11\bar{2}2)[11\bar{2}3]$ dislocation and (D–F) $(10\bar{1}1)[\bar{2}113]$ dislocation at the wurtzite-hexagonal phase boundary (highlighted by green dashed line). Atoms are color-coded by the atomic von Mises strain. The vector $[1\bar{1}0\bar{2}]$ is perpendicular to $[11\bar{2}0]$ on the pyramidal I plane, as defined in Figure 2A.

a $1/3\langle 11\bar{2}3 \rangle$ Burgers vector (6.195 Å). The corresponding critical resolved shear stress (CRSS) for nucleating the $[11\bar{2}3]$ dislocation on the pyramidal I and II planes at the phase boundary is 2.02 and 2.25 GPa, respectively. The CRSS values were determined to be $\tau = \sigma_{[0001]} \cos\phi \cos\lambda$, where $\sigma_{[0001]}$ is the magnitude of the applied compressive stress, ϕ is the angle between the normal of the slip plane and the direction of the applied force, and λ is the angle between the slip direction and the direction of the applied force. Approximately 10 dislocations are observed to nucleate in the nanopillar samples under compression (see Figure 5G). All dislocations originate from the phase boundary, with none nucleating directly from the surface. This suggests that the nucleation energy barrier for the phase transformation is significantly lower than that for dislocation nucleation from the surface. Consequently, the wurtzite-to-hexagonal phase transformation begins at the surface, followed by dislocation nucleation from the phase boundary. A similar mechanism has been observed in the compression of ceria nanocubes,[58] where the recrystallized phase serves as a structural seed for the nucleation of $1/6\langle 112 \rangle\{111\}$ partial dislocations. Once nucleated, the dislocation propagates across the entire

nanopillar samples as the compressive strain increases. These dislocations glide and encounter other formed dislocations. Each dislocation slip event results in a step on the nanopillar's surface (highlighted by the black arrows in Figure 3), contributing to a rougher surface texture.

To examine the size effect on the dislocation plasticity of nanopillars, we conducted simulations with cross-sectional diameters of 17 and 12 nm, while maintaining the same length-to-diameter ratio. The results, presented in Figure S3 of the Supporting Information, reveal that for models with a cross-sectional diameter exceeding 17 nm, the plastic deformation mechanism remains consistent: the wurtzite-to-hexagonal phase transformation begins at the surface, followed by dislocation nucleation from the phase boundary. In contrast, for models with diameters smaller than 12 nm, the behavior mirrors that of a unit cell, with no dislocation nucleation occurring even after the entire sample completes the phase transformation (see Figure S4 in the Supporting Information).

In addition to wurtzite GaN, we also study the dislocation plasticity of c-oriented ZnO nanopillars, which share the same wurtzite structure. The compression results of c-oriented ZnO nanopillars, presented in Figures S5–S10
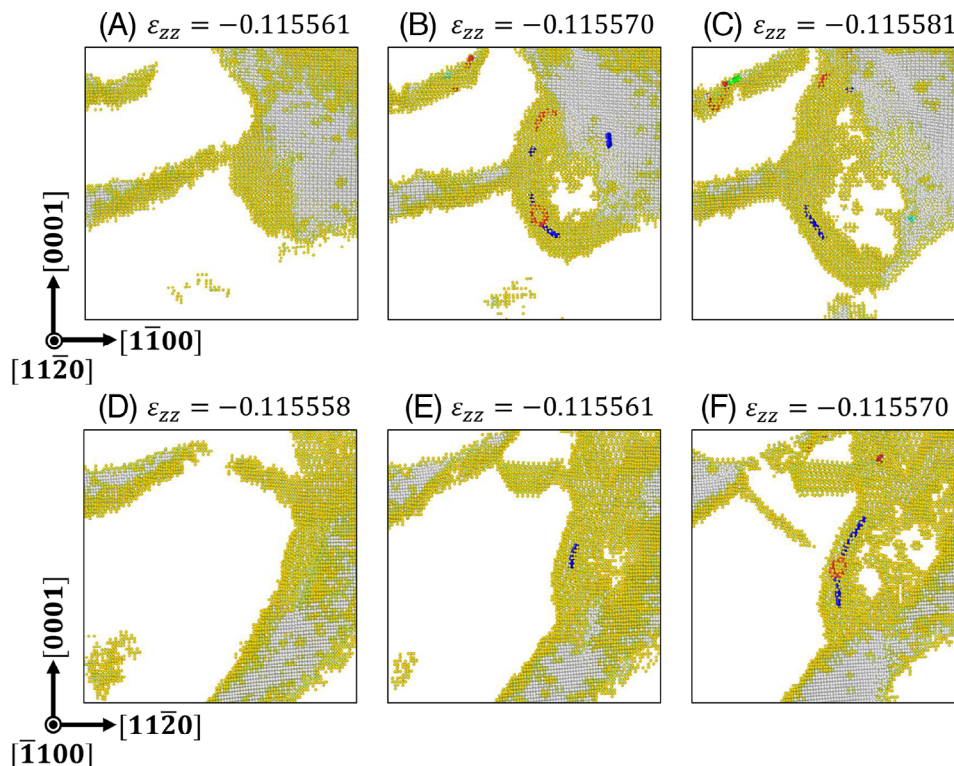
FIGURE 8 Slice view on the dislocation nucleation at wurtzite-to-hexagonal phase boundary on (A–C) pyramidal II plane and (D–F) pyramidal I plane, which appears in a half-loop configuration. Atoms are color-coded by the structure types analyzed via the Identify Diamond Structure (IDS) method.[32] To clarify, atoms on perfect wurtzite lattice are not shown. The dislocation configurations are analyzed by the Dislocation Extraction Algorithm (DXA)[33] based on the Ga HCP sublattice.

in the Supporting Information, indicate similar dislocation plasticity to that observed in GaN nanopillars. In both cases, $\{01\bar{1}1\}\langle11\bar{2}3\rangle$ and $\{11\bar{2}2\}\langle11\bar{2}3\rangle$ dislocations are activated during compression, with dislocations nucleating at the wurtzite-to-hexagonal phase boundary. It agrees with the experimental results that the 1-μm-diameter ZnO micropillars shears along the $(10\bar{1}1)$ plane that forms a 62° angle with respect to the (0001) basal plane under microcompression.[27] As shown in Figure S2a, the critical [0001] compressive engineering strain and peak stress at which the phase transformation initiates at the ZnO nanopillar surface are −0.1020 and −2.04 GPa, respectively. In comparison, the corresponding values calculated for a unit cell are −0.1600 for strain and −10.60 GPa for peak stress illustrated in Figure S4. The corresponding CRSS required to nucleate the $[11\bar{2}3]$ dislocation on the pyramidal I and II planes at the phase boundary is 0.82 and 0.91 GPa, respectively. Wang et al.[59] demonstrated, using the partially charged rigid ion model[60] as the interatomic potential, that a ZnO nanopillar can undergo a reversible wurtzite-to-hexagonal phase transformation throughout the entire sample at room temperature under uniaxial compressive strains of up to 22.1%. In contrast, our findings, based on the first-principles NNIP, reveal that the wurtzite-to-hexagonal phase transforma-

tion occurs locally, originating from the surface, under uniaxial compressive strains of up to 10.2%. With further deformation, dislocations are nucleated in the nanopillar samples. The result aligns with experimental observations of a similar reversible wurtzite-to-tetragonal reconstruction on ZnO $(10\bar{1}0)$ surfaces.[61] It is suggested that empirical potentials for ceramics might occasionally fall short in accurately simulating dislocation plasticity. In contrast, our NNIP, specifically designed for dislocation plasticity in ceramics,[30] offers a promising tool for modeling this phenomenon.

4 | SUMMARY

In this study, we carried out atomistic simulations to examine the dislocation plasticity in *c*-oriented GaN and ZnO nanopillars subjected to uniaxial compression along the [0001] direction. Our simulations made use of an innovative first-principles NNIP designed specifically for analyzing dislocation plasticity in ceramics. $\{01\bar{1}1\}\langle11\bar{2}3\rangle$ and $\{11\bar{2}2\}\langle11\bar{2}3\rangle$ dislocations were activated, consistent with observations from in-situ compression experiments. In detail, the wurtzite-to-hexagonal phase transformation starts at the facet edges, forming wedge-shaped regions,

and extends progressively inward. Under increased compression, dislocations nucleate at the boundary between the wurtzite and hexagonal phases and spread across the nanopillars, resulting in a rougher surface texture. These results offer new insights into the plastic deformation behaviors of GaN and ZnO nanopillars under compressive loading, highlighting the potential of dislocation engineering in these ceramics nanodevices.

ACKNOWLEDGMENTS

DECLARATION OF COMPETING INTEREST

The authors declare that they have no known competing financial interests or personal relationships that could have appeared to influence the work reported in this paper.

DATA AVAILABILITY STATEMENT

All the files used and/or constructed during the current study are available from the corresponding author upon reasonable request.

ORCID

Shihao Zhang https://orcid.org/0000-0001-9233-5163
Shigenobu Ogata https://orcid.org/0000-0002-9072-4496

REFERENCES

1. Nakamura A, Matsunaga K, Tohma J, Yamamoto T, Ikuhara Y. Conducting nanowires in insulating ceramics. Nat Mater. 2003;2(7):453–56.
2. Shibata N, Chisholm MF, Nakamura A, Pennycook SJ, Yamamoto T, Ikuhara Y. Nonstoichiometric dislocation cores in α-alumina. Science. 2007;316(5821):82–85.
3. Ikuhara Y. Nanowire design by dislocation technology. Prog Mater Sci. 2009;54(6):770–91.
4. Fang X, Nakamura A, Rödel J. Deform to perform: dislocation-tuned properties of ceramics. ACerS Bulletin. 2023;102(5):24–29.
5. Reddy KM, Guo D, Song S, Cheng C, Han J, Wang X, et al. Dislocation-mediated shear amorphization in boron carbide. Sci Adv. 2021;7(8):eabc6714.
6. Oshima Y, Nakamura A, Matsunaga K. Extraordinary plasticity of an inorganic semiconductor in darkness. Science. 2018;360(6390):772–74.
7. Sun B, Haunschild G, Polanco C, Ju J, Lindsay L, Koblmüller G, et al. Dislocation-induced thermal transport anisotropy in single-crystal group-iii nitride films. Nat Mater. 2019;18(2):136–40.
8. Höfling M, Zhou X, Riemer LM, Bruder E, Liu B, Zhou L, et al. Control of polarization in bulk ferroelectrics by mechanical dislocation imprint. Science. 2021;372(6545):961–64.
9. Zhuo F, Zhou X, Gao S, Höfling M, Dietrich F, Groszewicz PB, et al. Anisotropic dislocation-domain wall interactions in ferroelectrics. Nat Commun. 2022;13(1):6676.
10. Kissel M, Porz L, Frömling T, Nakamura A, Rödel J, Alexe M. Enhanced photoconductivity at dislocations in srtio3. Adv Mater. 2022;34(32):2203032.
11. Soulié A, Crocombette J-P, Kraych A, Garrido F, Sattonnay G, Clouet E. Atomistically-informed thermal glide model for edge dislocations in uranium dioxide. Acta Mater. 2018:150:248–61.
12. Madec R, Portelette L, Michel B, Amodeo J. Plastic anisotropy and composite slip: application to uranium dioxide. Acta Mater. 2023;255:119016.
13. Onofri C, Monchoux J, Amodeo J, Madec R, Sabathier C, Palancher H, et al. Versatility of dislocation motions in polycrystalline uo2 deformed at 1550∘ c investigated by tem. Scr Mater. 2024;244:116034.
14. Amodeo J, Maras E, Rodney D. Site dependence of surface dislocation nucleation in ceramic nanoparticles. npj Comput Mater. 2021;7(1):60.
15. Amodeo J, Lizoul K. Mechanical properties and dislocation nucleation in nanocrystals with blunt edges. Mater Des. 2017;135:223–31.
16. Issa I, Joly-Pottuz L, Amodeo J, Dunstan DJ, Esnouf C, Réthoré J, et al. From dislocation nucleation to dislocation multiplication in ceramic nanoparticle. Mater Res Lett. 2021;9(6):278–83.
17. Issa I, Amodeo J, Réthoré J, Joly-Pottuz L, Esnouf C, Morthomas J, et al. In situ investigation of mgo nanocube deformation at room temperature. Acta Mater. 2015;86:295–304.
18. Kim M, Seo J-H, Singisetti U, Ma Z. Recent advances in free-standing single crystalline wide band-gap semiconductors and their applications: Gan, sic, zno, β-ga 2 o 3, and diamond. J Mater Chem C. 2017;5(33):8338–54.
19. Pearton S. GaN and ZnO-based materials and devices. Vol. 156, Berlin: Springer Science & Business Media; 2012.
20. Nandi S, Kumar S, Misra A. Zinc oxide heterostructures: advances in devices from self-powered photodetectors to self-charging supercapacitors. Mater Adv. 2021;2(21):6768–99.
21. Fan S, Li X, Fan R, Lu Y. Size-dependent fracture behavior of gan pillars under room temperature compression. Nanoscale. 2020;12(45):23241–47.
22. Sung T, Huang J, Hsu J, Jian S. Mechanical response of gan film and micropillar under nanoindentation and microcompression. Appl Phys Lett. 97(17).
23. Wheeler J, Niederberger C, Tessarek C, Christiansen S, Michler J. Extraction of plasticity parameters of gan with high temperature, in situ micro-compression. Int J Plast. 2013;40:140–51.
24. Magagnosc DJ, Derenge MA, Jones KA. First formed dislocations in microcompressed c-oriented gan micropillars and their subsequent interactions. J Appl Phys. 128(4).

25. Oguri H, Li Y, Tochigi E, Fang X, Tanigaki K, Ogura Y, et al. Bringing the photoplastic effect in zno to light: a photoindentation study on pyramidal slip. J Eur Ceram Soc. 2024;44(2):1301–5.

26. Bradby J, Kucheyev S, Williams J, Jagadish C, Swain M, Munroe P, et al. Contact-induced defect propagation in zno. Appl Phys Lett. 2002;80(24):4537–39.

27. Sung TH, Huang JC, Hsu JH, Jian SR, Nieh TG. Yielding and plastic slip in zno. Appl Phys Lett. 2012;100(21):211903.

28. Gao P, Ishikawa R, Feng B, Kumamoto A, Shibata N, Ikuhara Y. Atomic-scale structure relaxation, chemistry and charge distribution of dislocation cores in srtio3. Ultramicroscopy. 2018;184:217–24.

29. Salamania J, Sangiovanni D, Kraych A, Kwick KC, Schramm I, Johnson L, et al. Elucidating dislocation core structures in titanium nitride through high-resolution imaging and atomistic simulations. Mater Des. 2022;224:111327.

30. Zhang S, Li Y, Suzuki S, Nakamura A, Ogata S. Neural network potential for dislocation plasticity in ceramics. npj Comput Mater. 2024;10(1):266.

31. Plimpton S. Fast parallel algorithms for short-range molecular dynamics. J Comput Phys. 1995;117(1):1–19.

32. Maras E, Trushin O, Stukowski A, Ala-Nissila T, Jonsson H. Global transition path search for dislocation formation in ge on si (001). Comput Phys Commun. 2016;205:13–21.

33. Stukowski A, Albe K. Extracting dislocations and non-dislocation crystal defects from atomistic simulation data. Model Simul Mater Sci Eng. 2010;18(8):085001.

34. Stukowski A. Visualization and analysis of atomistic simulation data with ovito–the open visualization tool. Model Simul Mater Sci Eng. 2009;18(1):015012.

35. Yao B, Zhang R, Aadis: an atomistic analyzer for dislocation character and distribution. Comput Phys Commun. 2020;247:106857.

36. Shimizu F, Ogata S, Li J. Theory of shear banding in metallic glasses and molecular dynamics calculations. Mater Trans. 2007;48(11):2923–27.

37. SQUID. https://www.hpc.cmc.osaka-u.ac.jp/squid/

38. Semlali E, Gil E, Avit G, André Y, Sauvagnat A, Jridi J, et al. Control of sag-gan at the nanoscale. Crystal Growth Des. 2024;24:8907.

39. Nami M, Stricklin IE, DaVico KM, Mishkat-Ul-Masabih S, Rishinaramangalam AK, Brueck S. Carrier dynamics and electro-optical characterization of high-performance gan/ingan core-shell nanowire light-emitting diodes. Sci Rep. 2018;8(1):501.

40. Jaloustre L, Ackermann V, De Mello SS, Labau S, Petit-Etienne C, Pargon E. Preferential crystal orientation etching of gan nanopillars in cl2 plasma. Mater Sci Semicond Process. 2023;165:107654.

41. He M-R, Zhu J. Defect-dominated diameter dependence of fracture strength in single-crystalline zno nanowires: in situ experiments. Phys Rev B Condens Matter Mater Phys. 2011;83(16):161302.

42. Agrawal R, Peng B, Espinosa HD. Experimental-computational investigation of zno nanowires strength and fracture. Nano Lett. 2009;9(12):4177–83.

43. Lee C, Feenstra RM, Northrup JE, Lymperakis L, Neugebauer J. Morphology and surface reconstructions of gan (1100) surfaces. Appl Phys Lett. 2003;82(11):1793–95.

44. Ding Y, Wang ZL. Profile imaging of reconstructed polar and non-polar surfaces of zno. Surf Sci. 2007;601(2):425–33.

45. Healy CJ, Ackland GJ. Molecular dynamics simulations of compression–tension asymmetry in plasticity of Fe nanopillars. Acta Mater. 2014;70:105–12.

46. Xie D, Chen M-J, Gigax J, Luscher D, Wang J, Hunter A. A fundamental understanding of how dislocation densities affect strain hardening behavior in copper single crystalline micropillars. Mech Mater. 2023;184:104731.

47. Jian S-R, Sung T-H, Huang J, Juang J-Y. Deformation behaviors of inp pillars under uniaxial compression. Appl Phys Lett. 101(15).

48. Schulz H, Thiemann K. Crystal structure refinement of aln and gan. Solid State Commun. 1977;23(11):815–19.

49. Lide D. CRC handbook of chemistry and physics. 89th ed. Boca Raton, FL: Taylor & Francis; 2008.

50. Zhang SH, Fu ZH. Zhang RF. Adais: automatic derivation of anisotropic ideal strength via high-throughput first-principles computations. Comput Phys Commun. 2019;238:244–53.

51. Kresse G, Furthmüller J. Efficient iterative schemes for ab initio total-energy calculations using a plane-wave basis set. Phys Rev B. 1996;54(16):11169.

52. Kresse G, Joubert D. From ultrasoft pseudopotentials to the projector augmented-wave method. Phys Rev B. 1999;59(3):1758.

53. Perdew JP, Burke K, Ernzerhof M. Generalized gradient approximation made simple. Phys Rev Lett. 1996;77(18):3865.

54. Methfessel MPAT, Paxton AT. High-precision sampling for brillouin-zone integration in metals. Phys Rev B. 1989;40(6):3616.

55. Monkhorst HJ, Pack JD. Special points for Brillouin-zone integrations. Phys Rev B. 1976;13(12):5188.

56. van de Walle A, Ceder G. Automating first-principles phase diagram calculations. J Phase Equilib. 2002;23(4):348–59.

57. Zhang SH, Zhang RF. Aelas: automatic elastic property derivations via high-throughput first-principles computation. Comput Phys Commun. 2017;220:403–16.

58. Laurens G, Amodeo J, Albaret T. Plastic deformations of ceria nanocubes under compression: an atomistic simulations study. Materialia. 2023;30:101824.

59. Wang J, Zhou M, Yang R, Xiao P, Ke F, Lu C. Repeatable mechanical energy absorption of zno nanopillars. Mater Today Commun. 2021;29:102904.

60. Wang S, Fan Z, Koster RS, Fang C, Van Huis MA, Yalcin AO, et al. New ab initio based pair potential for accurate simulation of phase transitions in zno. J Phys Chem C. 2014;118(20):11050–61.

61. He M-R, Yu R, Zhu J. Reversible wurtzite-tetragonal reconstruction in zno (1010) surfaces. Angew Chem. (International ed. in English). 2012;51(31):7744–47.

SUPPORTING INFORMATION

Additional supporting information can be found online in the Supporting Information section at the end of this article.